

# Correlation of Nanomorphology with Structural and Spectroscopic Studies in Organic Solar Cells

Urvashi Bothra, Nakul Jain, Amelia C. Y. Liu, Abhinav Kala, Wenchao Huang, Xuechen Jiao, Eliot Gann, Venu Gopal Achanta, Christopher R. McNeill,\* and Dinesh Kabra\*

Cite This: *ACS Appl. Nano Mater.* 2020, 3, 11080–11089

Read Online

ACCESS |

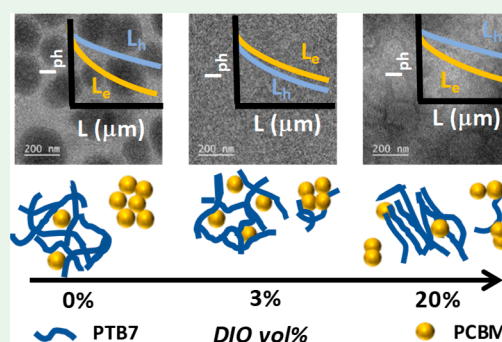
Metrics & More

Article Recommendations

Supporting Information

**ABSTRACT:** The nanomorphology of bulk heterojunction (BHJ) blends based on poly[[4,8-bis[(2-ethylhexyl)oxy]benzo[1,2-*b*:4,5-*b'*]dithiophene-2,6-diyl][3-fluoro-2-[(2-ethylhexyl)carbonyl]thieno[3,4-*b*]thiophenediyl]] (PTB7) blended with [6,6]-phenyl-C<sub>71</sub>-butyric acid methyl ester (PC<sub>71</sub>BM) is systematically varied by using the volume fraction of the solvent additive 1,8-diiodooctane (DIO) from 0 to 20 vol % in chlorobenzene to prepare organic solar cells (OSCs). Blends prepared without DIO forms large phase-separated domains of PC<sub>71</sub>BM which are suppressed on addition of 3 vol % DIO, resulting in improved nanoscale features. Addition of 20 vol % DIO results in a finer interconnected morphology along with increased roughness due to polymer aggregation, which contrasts with previous reports. With increase in addition of DIO the photoluminescence (PL) from the blend is reduced; however, a relative increase in PL from 750 nm onward is observed for blends with 20 vol % DIO. As quenching of the blend PL is related to the donor/acceptor interface, structural characterizations in real-space (microscopy) and *k*-space (scattering) are performed to unravel the nanomorphology and correlate it with photophysical and charge transport processes. Electron-transport length scales measured by scanning photocurrent microscopy are found to increase with the addition of up to 3 vol % DIO associated with the breakup of the large PC<sub>71</sub>BM agglomerates, while the hole-transport length is found to increase on adding DIO up to 20 vol % due to aggregation of polymer chains. Hence, this work represents a unique set of results systematically examining the effect of nanomorphology on structural and solar cells properties of BHJ blends, which can have a direct implication on better understanding of the emerging high-efficiency OSC systems.

**KEYWORDS:** organic solar cells, morphology, domain size, optical beam spread, spectroscopy



## 1. INTRODUCTION

The selection of a donor/acceptor material that can absorb a wide spectral range of the solar spectrum and form optimal nanoscale blend morphology is important to fabricate efficient organic solar cells.<sup>1–6</sup> To achieve the optimum morphology, the formation of phase-separated domains along with bicontinuous donor–acceptor pathways with domain size in the range of the exciton diffusion length (10–15 nm) is important.<sup>7</sup> Fine intermixing is important to facilitate charge generation (exciton dissociation), while phase-separated domains help in the efficient separation of charges from the donor/acceptor interface and the transport of free charge carriers to the electrodes.<sup>8–11</sup> In terms of prerequisites for the success of organic photovoltaics, the need of a detailed methodical structural and spectroscopic study of blends is paramount, which can correlate the role of nanomorphology to device physics in the organic solar cell (OSC) community.

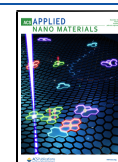
The nanoscale blend morphology in bulk heterojunction (BHJ) OSCs can be altered by thermal annealing, solvent annealing, varying the donor–acceptor ratio, altering the main and the side chain of the material, and adding a solvent

additive.<sup>12</sup> Recently, the addition of high boiling point solvent additives has been very useful in improving the efficiency of polymer/fullerene solar cells.<sup>13</sup> Solvent additives such as DIO and chloronaphthalene (CN) selectively dissolve one component and increase the drying time for film formation, facilitating the formation of an optimum morphology and leading to an improvement in the performance of the device.<sup>14–17</sup> The effect of the solvent additive varies for different donor–acceptor blend systems. We note that the DIO additive is used in this study to prepare various nanomorphologies of BHJ blends known to have a detrimental effect on stability aspects of devices.<sup>18–20</sup> It has been observed that the addition of DIO increases the domain size and forms purer fullerene and polymer domains in PCPDTBT:PC<sub>71</sub>BM

Received: August 20, 2020

Accepted: October 13, 2020

Published: October 27, 2020



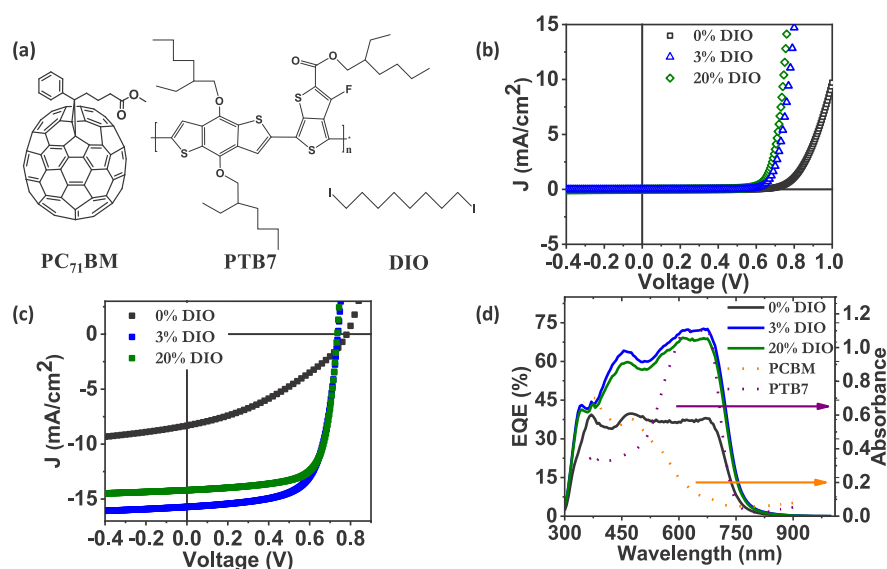


**Figure 1.** (a) Chemical structure of PC<sub>71</sub>BM, PTB7, and DIO, (b) dark  $J$ - $V$  characteristics, (c) illuminated  $J$ - $V$  characteristics under AM1.5 conditions, and (d) EQE of PTB7:PC<sub>71</sub>BM devices (ITO/PEIE/active layer/MoO<sub>3</sub>/Ag) with different vol % of DIO and absorbance spectra of pristine PTB7 and PC<sub>71</sub>BM thin film on a glass substrate.

blends, whereas, it decreases the size of PC<sub>71</sub>BM domains in PTB7:PC<sub>71</sub>BM systems while improving the morphology in both cases.<sup>1,21–25</sup> A detailed study of morphology by Collins et al. found that the addition of DIO reduces the size of fullerene domains by selectively dissolving PC<sub>71</sub>BM, which increases the interface in the PTB7:PC<sub>71</sub>BM blend without altering either the polymer or the fullerene composition.<sup>26</sup> Various studies on the effect of solvent additives on phase separation have proposed that in blends without an additive the liquid–liquid phase separation occurs before film drying which forms PC<sub>71</sub>BM agglomerates in the blend. However, on the addition of a high boiling point solvent additive, polymer aggregation and liquid–liquid phase separation occur at the same time, which leads to an intermixed morphology of the blend.<sup>27–29</sup>

In the study of Zusan et al., it was found that when 0–10 vol % of DIO is added to the PBDTTT-C:PC<sub>71</sub>BM system, the size of the polymer-rich domain increases. However, free charge carrier generation was found to decrease due to a reduction in the donor/acceptor interfacial area, which causes a decrease in the performance of the device.<sup>30</sup> In another study, Kim et al. suggested that the addition of DIO up to 8 vol % in the PTB7:PC<sub>71</sub>BM blend results in the reduction of the performance of the device due to reaggregation of PC<sub>71</sub>BM molecules in the blend matrix.<sup>31</sup> These two studies report conflicting results about the effect of excess DIO on the nanomorphology of polymer/fullerene blends, which could be due to the slightly different polymers used in the two studies that may have different PC<sub>71</sub>BM miscibilities. However, none of these studies quantitatively examined the domain size on adding different vol % of DIO in the blend. Therefore, a detailed insight into structural and spectroscopic studies is required to correlate the device operational mechanism with morphology in BHJ blends.

In this work, we have varied the nanomorphology of the PTB7:PC<sub>71</sub>BM blend by varying the DIO content systematically from 0 to 20 vol % in the host solvent. A correlation is established between the observed nanomorphology and device performance via structural studies and optoelectronic properties of the blend. Furthermore, structural studies are

complimented by high-resolution microscopic studies with an excellent agreement. The microscopic and spectroscopic studies were first performed on pristine PTB7 with different vol % of DIO and then on the blends with subsequent addition of DIO to understand the morphology of the blend. The blend without DIO has large PC<sub>71</sub>BM-rich domains and shows the least photoluminescence quenching due to less donor–acceptor interfacial area in such films. On adding 3 vol % of DIO, the electron transport length doubled with a 10-fold increase in electron mobility observed due to a reduction in the size of the PC<sub>71</sub>BM domains. On increasing DIO content to 20 vol %, agglomeration of the polymer PTB7 was observed, which led to increased hole transport length, hole mobility, and fill factor (FF) in the devices. As per the literature, such a unique set of results on BHJ blend in OSC community is unprecedented, where structural, spectroscopic, microscopic, and charge transport studies are put up together with a remarkable coherence.

## 2. RESULTS

**Device Characteristics.** Figure 1a presents the molecular structures of PTB7, PC<sub>71</sub>BM, and DIO. Solar cells were fabricated with an inverted architecture of indium tin oxide (ITO)/polyethylenimine ethoxylated (PEIE)/PTB7:PC<sub>71</sub>BM/MoO<sub>3</sub>/Ag. The energy level diagram and the schematic of the device architecture are shown in Figure S1. Devices were prepared with different vol % of DIO (0%, 1%, 3%, 10%, and 20%) in the casting solution with chlorobenzene (CB) used as the majority solvent. The vol % values quoted reflect the vol % of DIO in the total solution volume. A PTB7:PC<sub>71</sub>BM weight ratio of 1:1.5 was maintained along with a total concentration of polymer and fullerene of 25 mg/mL. Device performance was obtained by measuring current density–voltage ( $J$ - $V$ ) characteristics and external quantum efficiency (EQE). The film thickness for blends with 0, 1, 3, 10, and 20 vol % of DIO measured by a Dektak profilometer are 108, 93, 94, 101, and 131 nm, respectively. The dark and illuminated  $J$ - $V$  characteristics for blends with 0, 3, and 20 vol % of DIO are shown in Figures 1b and 1c, respectively. Figure S2 represents dark  $J$ - $V$ ,

Table 1. Device Performance Parameter Extracted from  $I$ - $V$  Characteristics and EQE Measurements<sup>a</sup>

|                   | $V_{OC}$ (V) | $J_{SC}$ (mA/cm <sup>2</sup> ) | FF (%) | efficiency (%) | $J_{SC}$ from EQE (mA/cm <sup>2</sup> ) |
|-------------------|--------------|--------------------------------|--------|----------------|---|
| PTB7:PCBM 0% DIO  | 0.77 ± 0.01  | 8.4 ± 1.0                      | 33 ± 2 | 2.0 ± 0.3      | 8.39                                    |
| PTB7:PCBM 1% DIO  | 0.76 ± 0.01  | 14.1 ± 0.7                     | 50 ± 2 | 5.1 ± 0.8      | 13.7                                    |
| PTB7:PCBM 3% DIO  | 0.74 ± 0.01  | 15.7 ± 0.4                     | 67 ± 2 | 7.7 ± 0.3      | 14.9                                    |
| PTB7:PCBM 10% DIO | 0.73 ± 0.01  | 15.6 ± 0.4                     | 67 ± 4 | 7.6 ± 0.4      | 14.5                                    |
| PTB7:PCBM 20% DIO | 0.73 ± 0.01  | 14.3 ± 0.4                     | 70 ± 2 | 7.3 ± 0.4      | 14.0                                    |

<sup>a</sup>Uncertainties are standard deviation of multiple ( $\approx 10$ ) samples. <sup>b</sup>Average of 10 devices.

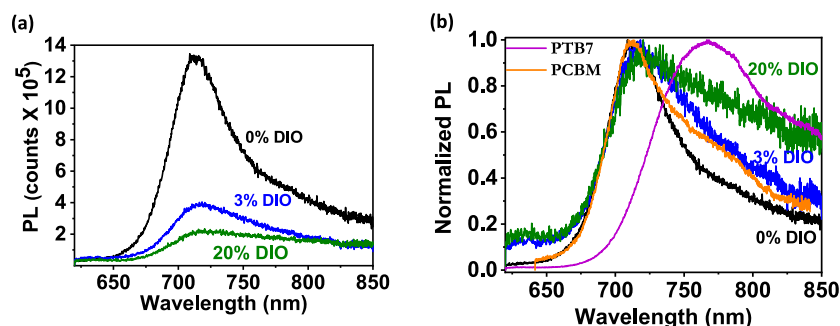


Figure 2. (a) Photoluminescence spectra of PTB7:PC<sub>71</sub>BM blend films with different DIO vol %. (b) Normalized PL spectra for the blends and pristine materials. The excitation source is a 490 nm diode laser.

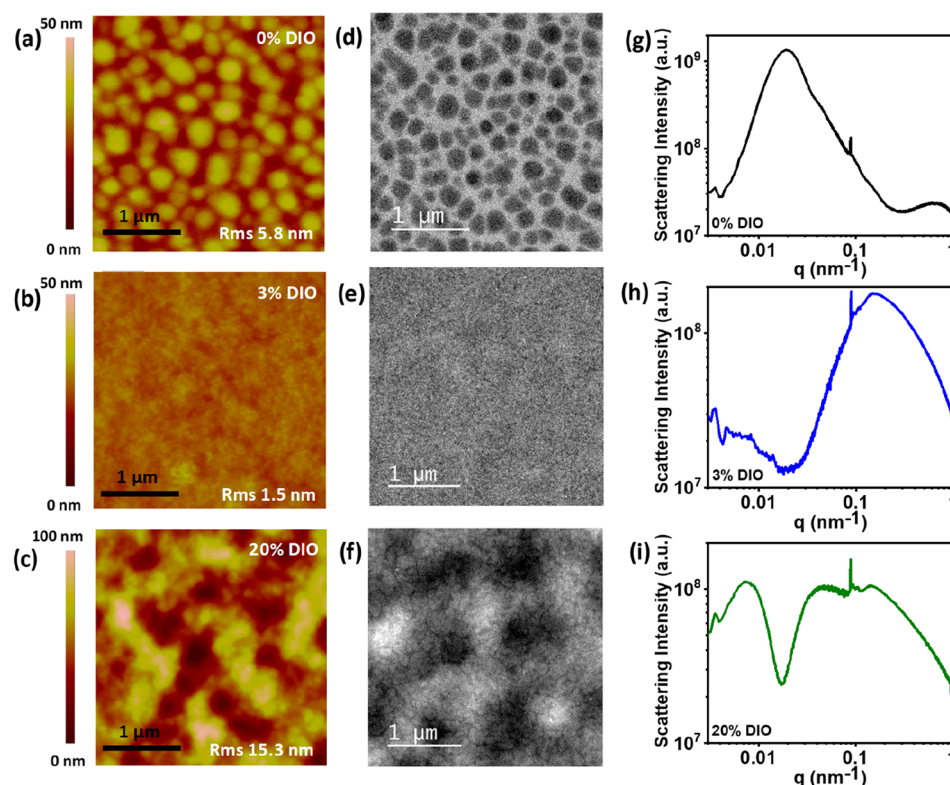


Figure 3. AFM height images for PTB7:PC<sub>71</sub>BM blend without DIO (a), 3 vol % DIO (b), and 20 vol % DIO (c). Bright-field TEM images for blends without DIO (d), 3 vol % DIO (e), and 20 vol % DIO (f). Lorentz-corrected RSoXS profiles for PTB7:PC<sub>71</sub>BM blends with 0 vol % (g), 3 vol % (h), and 20 vol % (i). The length scale for AFM and TEM images is  $3 \mu\text{m} \times 3 \mu\text{m}$ .

illuminated  $J$ - $V$ , and EQE for blends with all five different vol % of DIO. A decrease in the knee voltage as well as the open-circuit voltage ( $V_{OC}$ ) was observed in devices prepared with DIO (Figure S3 and Figure 1c). The decrease in knee voltage is related to delocalization of electronic states, and it has been observed in other polymer systems as well.<sup>21,32</sup> The device performance increased from 2% to 5% on adding even 1 vol %

of DIO. This steep improvement is due to a significant improvement in the short-circuit current density ( $J_{SC}$ ) and the FF of the device. The best device performance was obtained for blends with 3 vol % DIO, and the device performance was similar when DIO was added up to 20 vol %. However, a decrease in the  $J_{SC}$  and increase in FF were observed when 20 vol % of DIO was added. Figure 1d shows the EQE for devices

with different vol % of DIO, and a significant increase in EQE is seen at the PTB7 absorption region on adding DIO to the blend. Table 1 shows device performance parameters such as  $J_{SC}$ ,  $V_{OC}$ , FF, power conversion efficiency (PCE) and  $J_{SC}$ , which is calculated from EQE.

**Spectroscopic Studies.** UV–vis absorption spectra for pristine PTB7 and PC<sub>71</sub>BM films are shown in Figure 1d. Figure 2a represents the PL spectra of blends with 0%, 3%, and 20 vol % of DIO, and PL of blends with 1% and 10% DIO is shown in Figure S4. The PL spectrum was recorded by exciting the film with a 490 nm diode laser where the absorption of both PTB7 and PC<sub>71</sub>BM takes place in the blend film. PL spectra of the blends have a peak at 710 nm and were maximum for films without DIO. PL quenching was observed on adding DIO, which suggests an increase in interfacial area between donor and acceptor for blend films that contain solvent additive. Figure 2b shows the normalized PL spectra for pristine materials as well as the blends. The PL spectra of the blend resemble the spectrum of pure PC<sub>71</sub>BM, which signifies radiative decay of the photon which is absorbed by the PC<sub>71</sub>BM. When 10 and 20 vol % of DIO are added, a relative increase in the photoluminescence from PTB7 region was observed which could indicate reduced quenching of excitons generated in the polymer phase due to increased PTB7 aggregation in the blend matrix. A decrease in the PL at 710 nm is observed along with relative increase in PL at 780 nm for blends with 20 vol % DIO, which could be due to finer mixing of PC<sub>71</sub>BM in PTB7 matrix. Figure S16 shows the UV–vis absorption spectra of PTB7 in solution and in solid film with different vol % of DIO in the host solvent. The solution spectra of PTB7 with different DIO concentrations in CB are identical; however, an increased  $A_{0-1}$  absorption peak is observed for PTB7 solid films on the addition of DIO.

**Morphological and Structural Studies.** Figure 3a–c shows the atomic force microscopy (AFM) images, Figure 3d–f shows the transmission electron microscopy (TEM) images, and Figure 3g–i shows the resonant soft X-ray scattering (R-SoXS) profiles for the blends with 0, 3, and 20 vol % of DIO. Full data sets including the 1 and 10 vol % samples can also be found in the Supporting Information. Phase images of AFM for the blends are shown in Figure S5. The blend film processed without DIO is characterized by large, phase-separated domains of PC<sub>71</sub>BM surrounded by a mixed polymer/fullerene matrix, borne out by the AFM, TEM, and R-SoXS data. The AFM data of the 0 vol % sample show height variations on a length scale of  $\approx 300$  nm, which is consistent with the average lateral size of the PC<sub>71</sub>BM domains measured with a TEM of  $\approx 240$  nm. (Figures S8 and S9 show the comparison of domain size measured from the AFM and TEM measurements for 0 and 20 vol % DIO, and the methodology for measuring the domain size is also presented.) The R-SoXS profile for the 0 vol % sample has a peak at  $\approx 0.02$  nm<sup>-1</sup>, which corresponds to a spatial fluctuation of  $\approx 300$  nm and is furthermore consistent with the AFM and TEM data.

With the addition of 3 vol % DIO the surface roughness decreases from 5.8 to 1.5 nm. The TEM image also shows a dramatic change in morphology with a much finer intermixing of donor and acceptor. Although measurement of domain size from the AFM and TEM images of the 3 vol % sample is difficult, the R-SoXS profile of this sample shows a peak at  $\approx 0.15$  nm<sup>-1</sup>, consistent with a spatial fluctuation of  $\approx 40$  nm. The R-SoXS profile of the 3 vol % sample is still broad, indicating a distribution of length scales; however, the R-SoXS

profile is dramatically shifted to the right (toward higher  $q$  and smaller spatial fluctuations), consistent with the suppression of oversized phase and consistent with the results of Collins et al.<sup>26</sup> Increasing the amount of DIO in the casting solution to 20 vol % results in a dramatic increase in film roughness to 15.3 nm. The blend film with 20 vol % DIO is thicker than the other films, but the effect of thickness on the blend morphology can be considered very less as seen in previous study.<sup>33</sup> Examining the effect of DIO concentration on film roughness and AFM morphology indicates that the film roughness in the 20 vol % PTB7:PC<sub>71</sub>BM sample is not due to phase separation but rather due to the effect of a high concentration of DIO on film roughness, likely caused by polymer aggregation during drying due to low solubility of PTB7 in DIO.<sup>34,35</sup> Interestingly the TEM image reveals additional structure characterized by an interconnected darker phase with a finer domain size as compared to the spatial variation seen with AFM. The R-SoXS data confirm the hierarchical nature of the 20 vol % DIO sample with scattering features apparent at  $\approx 0.15$ ,  $\approx 0.05$ , and  $\approx 0.0075$  nm<sup>-1</sup>. The feature at  $\approx 0.15$  nm<sup>-1</sup> is consistent with smaller fullerene-rich domains with size  $< 50$  nm as observed in the 3 vol % sample,<sup>26</sup> the  $\approx 0.05$  nm<sup>-1</sup> feature corresponds to a spatial fluctuation of  $\approx 125$  nm consistent with the darker interconnected phase observed with TEM, and the feature at  $\approx 0.0075$  nm<sup>-1</sup> corresponds to a spatial fluctuation of  $\approx 850$  nm consistent with the film roughness observed in AFM and contrast variation in TEM images. Again, the features in R-SoXS are quite broad, indicating a wide distribution of feature sizes, with AFM and TEM data helping to elucidate and confirm the hierarchical nature of the morphology. Table 2 summarizes the

**Table 2. Domain Size Measured from AFM, TEM, and Spatial Fluctuations from R-SoXS for the PTB7:PC<sub>71</sub>BM Blend with 0, 3, and 20 vol % DIO<sup>a</sup>**

| vol % DIO                  | domain size by AFM (nm) | domain size by TEM (nm) | spatial fluctuations from R-SoXS (nm) |
|----------------------------|-------------------------|-------------------------|---------------------------------------|
| 0% DIO                     | 250 ± 85                | 240 ± 60                | 300                                   |
| 3% DIO                     |                         |                         | 40                                    |
| 20% DIO (fine structure)   |                         | 140 ± 45                | 125                                   |
| 20% DIO (coarse structure) | 740 ± 85                | 700 ± 60                | 850                                   |

<sup>a</sup>Uncertainties are standard deviation of multiple (>10) samples.

domain sizes determined for blends with 0, 3, and 20 vol % DIO. The 1 vol % sample shows features that are intermediate to the 0 and 3 vol % samples, and similarly the 10 vol % sample shows features intermediate between the 3 and 20 vol % samples, indicating a continuous evolution in morphology with increasing DIO content.

To investigate the effect of DIO on the molecular orientation and polymer packing, near-edge X-ray absorption fine structure (NEXAFS) spectroscopy and grazing-incidence wide-angle X-ray scattering (GIWAXS) are performed. Figures S18 and S19 show the angle-resolved carbon K-edge total electron yield (TEY) NEXAFS spectra for pristine materials and blends, respectively. Tilt angles calculated for all the systems are summarized in Table S2. Very little or only slight dichorism is observed for the C 1s– $\pi^*$  transition in pristine PTB7 films, indicating that DIO has little effect on the orientation of polymer chains at the top surface with PTB7

chains in general adopting a rather isotropic orientation at the surface. A similar lack of dichroism is seen for the PTB7:PC<sub>71</sub>BM blends. By comparing the TEY NEXAFS spectra of the surface of the blends with neat spectra, we determined the surface composition of the blends by compositional fitting, as shown in Figure S20. A slight decrease in PTB7 composition at the surface was found, dropping from ≈60 wt % for the 0 vol % sample to ≈53 wt % for 1, 3, and 10 vol % and ≈55 wt % for 20 vol %, signifying that the blend surface without DIO is slightly richer in PTB7. Figure S21 shows GIWAXS 2D images and 1D out-of-plane and in-plane line profiles. A prominent (100) reflection is found at  $q = 0.35 \text{ \AA}^{-1}$  along the in-plane direction, corresponding to the polymer alkyl stacking. Moreover, with the increase of DIO concentration, the polymer (100) scattering peak becomes slightly narrower, suggesting a larger coherence length. The coherence length is measured by fitting PTB7 (100) peak by the Scherrer equation and is represented in Table S3.<sup>36</sup> No significant change is observed in the coherence length for samples with different DIO percent in the host solvent.

**Effective Transport Lengths and Mobility.** In this section, we investigate the correlation in charge transport/carrier mobility with the morphology of the donor–acceptor blend. Electron-only and hole-only devices are prepared with the device architecture of ITO/PEIE/PTB7:PC<sub>71</sub>BM/Ca/Al and ITO/PEDOT:PSS/PTB7:PC<sub>71</sub>BM/MoO<sub>3</sub>/Au, respectively. The mobility was calculated by fitting  $J$ – $V$  curves of single carrier devices with the Mott–Gurney equation which is written as

$$J = \frac{9}{8} \epsilon \mu (V - V_{\text{bi}})^2 \exp(g \sqrt{V - V_{\text{bi}}}) / d^3$$

where  $V_{\text{bi}}$  is the built-in potential,  $\epsilon$  is the permittivity, and  $g = \beta/\sqrt{d}$ , where  $\beta$  is the Poole–Frenkel coefficient and  $d$  is the film thickness.<sup>32</sup> The electron mobility for devices without DIO is  $4.8 \times 10^{-5} \text{ cm}^2/(\text{V s})$ , which increased to  $7.9 \times 10^{-4} \text{ cm}^2/(\text{V s})$  when 3% of DIO is added to the blend. On the other hand, the hole mobility decreased on adding 3 vol % of DIO in the blend and increased again on addition of 20 vol % DIO. The electron and hole mobility values for devices with and without 3 vol % DIO are consistent with the previous reports.<sup>37,38</sup> Figure S11 shows the  $J$ – $V$  curves with Poole–Frenkel fitting for the blends, and the fitting parameters are given in Table S1. Table 3 shows the mobility and effective transport lengths for all combinations of blends.

To understand the effect of the concentration of DIO on the charge transport, effective transport lengths ( $L$ ) are measured by using scanning photocurrent microscopy (SPM). Setup for

the SPM is shown in Figure S12a, and the experimental details are mentioned in the section on methodology. To measure the electron transport length ( $L_e$ ), the laser is focused on the pixel (active area region where both Ag and ITO are present) and is scanned from that pixel to beyond the ITO region such that the Ag electrode is present, and the schematic is shown in Figure 4a. When the laser spot moved away from the pixel, the

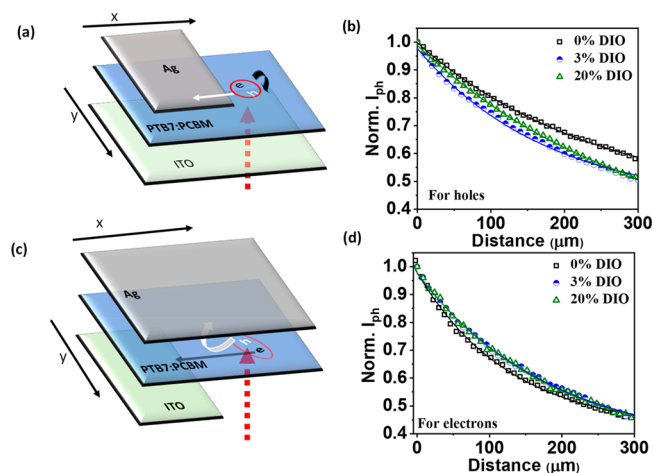


**Figure 4.** Schematic of scanning photocurrent microscopy showing the lateral transport of (a) holes and (c) electrons. Photocurrent vs scanning distance for (b) holes and (d) electrons in PTB7:PC<sub>71</sub>BM blend devices fabricated with different DIO vol %. Solid line is fit to experimental data to determine the effective transport lengths by fitting with monoexponential decay.

generated holes are collected by the Ag present beneath the active layer, but the electron needs to be collected by ITO by lateral transport of electrons. Thus, the transport lengths ( $L_e$ ) are measured by the phenomenon of the lateral photovoltaic effect.<sup>39</sup> Similarly, to measure the hole transport length ( $L_h$ ), scanning is performed from the pixel to beyond the Ag electrode as shown in Figure 4c. The phase and amplitude of photocurrent are recorded as a function of the position in the lock-in amplifier (Figure S12b). The figure is divided in three different regions, which shows scanning on the active area, the intermediate region, and the region completely outside the electrode. The region completely outside one of the electrodes is a low electric field regime, and therefore in this region the diffusion process is effective for the photoinduced charge carriers which are dependent on the blend semiconductor property.

To understand whether the waveguiding effects in the thin film can affect the transport length due to different roughness of semiconductor, FDTD simulations are carried out. The details of the simulation are mentioned in the experimental section. Figure S13 shows the schematic of structure and excitation source used in simulation. The electric field profile at the center of semiconductor and ITO are shown in Figures S14a and S14b, respectively. These electric field profiles indicate that the field is mostly confined near the focal spot, and not much of the field is leaking away from that into the guided modes. The loss rate for the fundamental TM mode ( $4.0413 \times 10^5 \text{ dB/cm}$ ) and for the fundamental TE mode ( $1.3887 \times 10^5 \text{ dB/cm}$ ) calculated by using the mode source is very significant, and therefore that could be reason for the insignificant energy transfer in the lateral direction away from the spot. The simulations were also performed at the ITO/

**Table 3. Electron Mobility, Hole Mobility, Electron Transport Length, and Hole Transport Length for Blends with Different vol % of DIO<sup>a</sup>**

| % DIO | hole mobility (cm <sup>2</sup> /(V s)) | electron mobility (cm <sup>2</sup> /(V s)) | hole transport length (μm) | electron transport length (μm) |
|-------|--|--|----------------------------|--------------------------------|
| 0     | $9.1 \times 10^{-4}$                   | $4.8 \times 10^{-5}$                       | $251 \pm 4$                | $128 \pm 2$                    |
| 1     | $2.7 \times 10^{-4}$                   | $2.0 \times 10^{-4}$                       | $241 \pm 3$                | $153 \pm 4$                    |
| 3     | $4.5 \times 10^{-4}$                   | $7.9 \times 10^{-4}$                       | $178 \pm 7$                | $184 \pm 3$                    |
| 10    | $5.6 \times 10^{-4}$                   | $8.5 \times 10^{-4}$                       | $305 \pm 7$                | $189 \pm 4$                    |
| 20    | $2.0 \times 10^{-3}$                   | $3.2 \times 10^{-4}$                       | $298 \pm 8$                | $181 \pm 4$                    |

<sup>a</sup>Uncertainties are standard deviation of multiple (>5) samples.

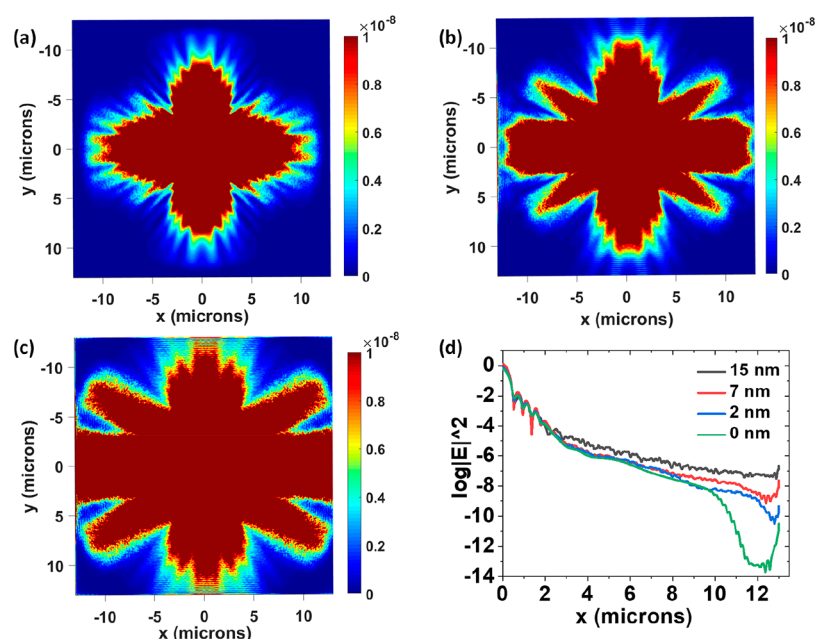


**Figure 5.**  $|E|^2$  plot for semiconductor with (a) 2, (b) 7, and (c) 15 nm surface roughness for a 26  $\mu\text{m}$  simulation size at the ITO/semiconductor interface. The ITO surface roughness is 1.8 nm. (d)  $|E|^2$  line plot along the  $x$ -axis for different roughness of semiconductor. The distance is measured from the center of focused laser beam. The units of the electric field are V/m.

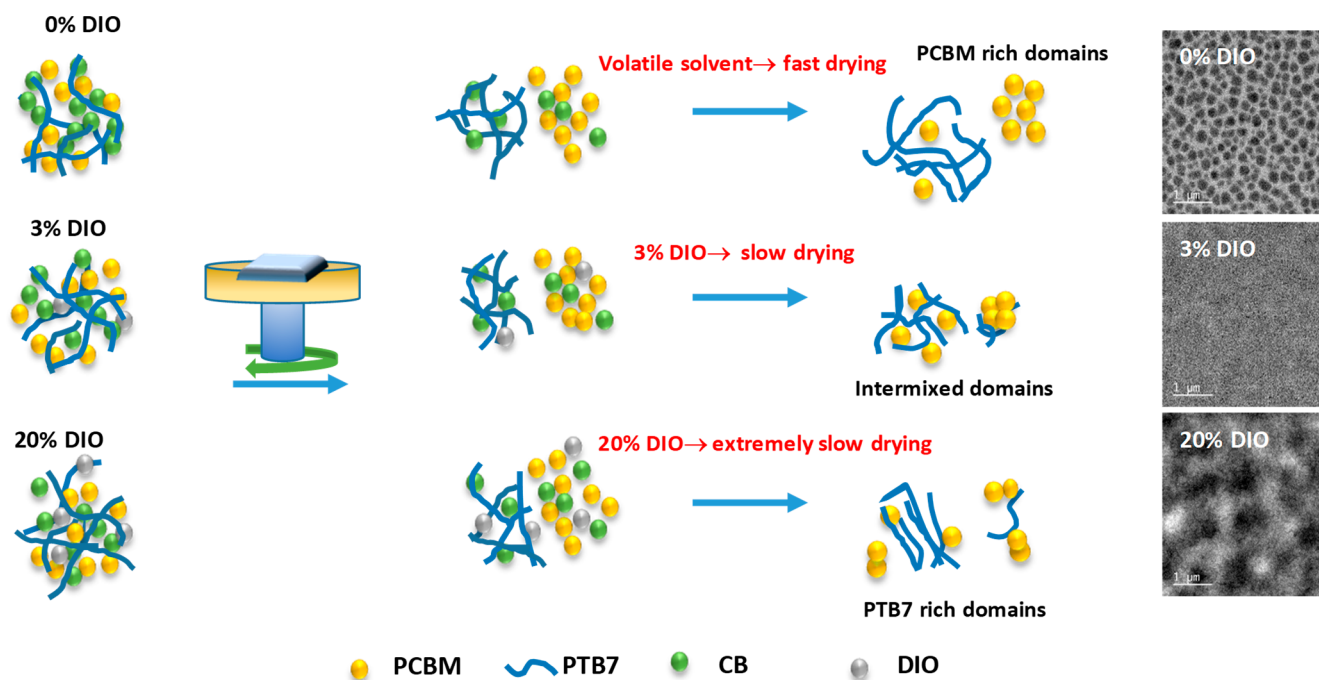


**Figure 6.** Schematic of PTB7/PC<sub>71</sub>BM blend with different solvents. The figure shows phase separation after spin-coating and final morphology after drying of the solvent additive (DIO). The proposed morphology is compared with the TEM images for blends with 0, 3, and 20 vol % DIO.

semiconductor interface while considering the roughness of ITO and semiconductor film. Figure 5 shows the electric field plot for different semiconductor roughness along with the line plot of field in  $x$  direction. From the simulations, it is evident that the film roughness helps the field to propagate relatively larger distance compared to film without any roughness. For the film with roughness of 15 nm, the field strength is 1 order of magnitude higher than the film with 7 nm roughness at a 12  $\mu\text{m}$  distance from the center. Therefore, the films with higher roughness can result in slightly larger transport lengths due to

the contribution of optical beam spread. The photocurrent ( $I_{\text{ph}}$ ) values as a function of the position outside the pixel is fitted by the equation  $n(x) = n_0 \exp(-x/L)$ .<sup>21,40</sup> The normalized lateral hole  $I_{\text{ph}}$  and lateral electron  $I_{\text{ph}}$  as a function of the scanning distance away from the pixel for blends with 0, 3, and 20 vol % DIO are shown in Figures 4b and 4d, respectively. The  $L_s$  for blends with 1 and 10 vol % DIO is shown in Figure S15. The mobility and transport lengths show correlation with the change in morphology from PCBM agglomerated domains to PTB7 aggregated chains. However, a

slight variation in the correlation of mobility and  $L_s$  could be due to known anisotropic charge transport properties in vertical and lateral direction, respectively, and increase in the lateral spread of light for rougher films.<sup>41</sup> The  $L_e$  increased from 128 to 184  $\mu\text{m}$  when 3 vol % of DIO is added and did not change on adding further DIO to the blend. However, the  $L_h$  decreased from 251 to 178  $\mu\text{m}$  when 3 vol % of DIO is added and increased to 298  $\mu\text{m}$  at 20 vol % of DIO in CB.

### 3. DISCUSSION

The morphology of bulk heterojunction organic solar cells affects the charge generation, transport, and recombination; therefore, the optimum morphology is important in the power conversion efficiency of devices. The efficiency of PTB7:PC<sub>71</sub>BM devices prepared without DIO is only 2% due to a low FF of 33% and a current density of 8.4 mA/cm<sup>2</sup>. Figure 3 shows that the PC<sub>71</sub>BM domain size is reduced on addition of DIO in the blend. The addition of even 1 vol % DIO to the PTB7:PC<sub>71</sub>BM blend breaks down the fullerene agglomerates into smaller domains of PC<sub>71</sub>BM, confirmed by the AFM, TEM, and R-SoXS results shown in the Supporting Information, resulting in increased current density from PTB7 as well as PC<sub>71</sub>BM absorption region due to improved charge transfer and interconnecting path. The absorption spectra of PTB7 in solution and in solid film as shown in Figure S16 imply that PTB7 in solution phase with up to 10 vol % of DIO does not show any improved aggregation, and the change in PTB7 film morphology takes place during the film drying. Moreover, because of less solubility of PTB7 in DIO, PTB7 films with 20 vol % of DIO show increased roughness and aggregation due to self-assembly of the polymer during the slow evaporation of the high boiling point solvent additive, which also increases PL around 780 nm.<sup>42</sup>

Figure 6 shows a schematic diagram of morphology evolution at all the stages from blend solution until film drying. The PTB7:PC<sub>71</sub>BM blend with only CB dries after spin-coating and results in liquid–liquid phase separation due to the low boiling point of CB, resulting in the morphology of large PCBM-rich domains and PTB7/PCBM mixed matrix phase (rich in PTB7). On adding 3 vol % of DIO, the large PC<sub>71</sub>BM domain dissolves in the additive due to its high solubility and results in intermixed domains because of slow drying which results in the quenching of PL from the blend. Addition of 20 vol % of DIO increases the drying time of film further and results in PTB7 aggregation in the film and a coarse feature due to its limited solubility in DIO, which is similar to the morphology observed by Yu et al. in the polymer–polymer system.<sup>43</sup> The predicted morphology after film drying for 0, 3, and 20 vol % DIO is compared with the TEM images. The coarse features observed in the blend prepared with 20 vol % DIO is due to the film roughness which is comparable to the AFM images of pristine PTB7 (Figure S7). The TEM image of blend with 20% DIO at higher magnification, as shown in Figure S17, shows PTB7-rich domains with a lateral thickness of  $\approx 140$  nm. Scattering due to fine and coarse feature is also observed in the R-SoXS profiles as discussed above. The PTB7-rich domains may contribute to enhanced hole transport in the devices.

To investigate the effect of fullerene dispersion on the  $J_{sc}$  and FF, the charge carrier mobility and transport lengths are characterized. The electron mobility increased by an order of magnitude, and the electron transport length increased from 128 to 184  $\mu\text{m}$  on incorporating DIO into the blend. It is

evident from the mobility values and the PL quenching that the increase in the device performance from 2% to 7.6% is due to better distribution of PC<sub>71</sub>BM domains in the blend, which forms interconnecting pathways and facilitates charge transport.<sup>37</sup> The electron mobility and electron transport lengths are found to be correlated to each other and are maximum for devices with 3 vol % DIO. Unlike the increase in electron mobility and transport length, the hole mobility and  $L_h$  decreased slightly when DIO is added to the blend and then increased on subsequent addition of DIO up to 20 vol %. The increase in hole mobility when 10 and 20 vol % of DIO are added is due to the increased aggregation of PTB7. Therefore, the drastic improvement in the performance of devices from 0 to 3 vol % is due to better electron transport in the blend because of optimum domain size and better distribution of PC<sub>71</sub>BM in the blend matrix. On the addition of DIO above 3 vol %, PTB7 forms aggregates in the blend along with interconnected network between PTB7 and PCBM which leads to better charge transport. However, a slight decrease in device current is observed which could be due to decrease in proximity of PTB7 with pure PC<sub>71</sub>BM domains due to finer morphology.

### 4. CONCLUSION

We have modulated the bulk heterojunction morphology with domain size ranging from 10s of nm to 100s of nm to present a unique set of results by correlating the nanostructural packing with the spectroscopic and electrical characterization for organic solar cells. The blend film processed without DIO forms large fullerene-rich domains which have few donor–acceptor interfaces, resulting in poor exciton dissociation and a low PCE of 2%. When DIO is added to the PTB7:PC<sub>71</sub>BM blend, large PC<sub>71</sub>BM domains break down into smaller pure domains, which improves the nanoscale morphology, resulting in improved charge transfer, electron mobility, and electron transport lengths. AFM, TEM, and R-SoXS were used to characterize the film morphology. The addition of 3 vol % DIO was found to reduce the domain size from  $\approx 300$  to  $\approx 40$  nm, with a further increase of DIO to 20 vol %, resulting in a hierarchical morphology with thickness variation on the length scale of  $\approx 800$  nm, an intermediate interconnected morphology on the  $\approx 200$  nm length scale, and finer fullerene-rich domains. Unlike earlier observations, we find that on increasing the DIO content higher than 3 vol % in the blend, PTB7 chains aggregate instead of PC<sub>71</sub>BM because of the low solubility of PTB7 in DIO and increase in self-assembly time, which improves the hole mobility in this blend system. The structural results are found to be in good agreement with the PL quenching and the effective transport lengths. Therefore, an evolution in the morphology from fullerene-rich domains to polymer-rich domains is observed in the PTB7:PC<sub>71</sub>BM blend without DIO and with 20 vol % of DIO, respectively in the host solvent.

### 5. EXPERIMENTAL SECTION

**Device Fabrication.** PTB7 (donor) and PC<sub>71</sub>BM (acceptor) were purchased from 1-material and Solenne BV, respectively, and were used as-received. (Certain commercial equipment, instruments, or materials are identified in this paper to foster understanding. Such identification does not imply recommendation or endorsement by the National Institute of Standards and Technology, nor does it imply that the materials or equipment identified are necessarily the best available for the purpose.) PEIE, CB, and 2-methoxyethanol were

purchased from Sigma-Aldrich. The device was fabricated with an inverted architecture of ITO/PEIE/PTB7:PC<sub>71</sub>BM/MoO<sub>3</sub>/Ag. ITO-coated glass was purchased from Lumtec and sonicated in soapy water, deionized water, acetone, and isopropyl alcohol for 10 min each. The cleaned glass after drying with nitrogen was then placed in a plasma asher for 10 min to improve the wettability of substrates. A PEIE solution with 0.4 wt % in 2-methoxyethanol was stirred overnight and spin-coated on the ITO substrates at 6000 rpm for 50 s; it was subsequently annealed at 110 °C for 10 min. After deposition of the electron transport layer (ETL), the substrates were kept inside a nitrogen glovebox. PTB7:PC<sub>71</sub>BM solutions with different vol % of DIO were prepared at 1:1.5 by weight with an overall concentration of 25 mg/mL in CB. The solution was stirred overnight at 65 °C, and a different volume of DIO was added in the solution 15 min before spin-coating. PTB7:PC<sub>71</sub>BM solutions were spin-coated at 2000 rpm for 1 min and then kept in a vacuum for 1 h to dry the films. The PTB7:PC<sub>71</sub>BM spin-coated samples were then transferred to the thermal evaporator to deposit 15 nm of MoO<sub>3</sub> and 100 nm of Ag at 3 × 10<sup>-6</sup> mbar onto it. The devices were then encapsulated by epoxy resin from Devcon 2-Ton inside the glovebox.

**Film Characterization.** For UV-vis spectroscopy and photoluminescence spectroscopy, the glass and quartz substrates, respectively, were cleaned by the same procedure as mentioned in the above section. PEIE was spin-coated on the substrates, and subsequently, the blend solution with different DIO vol % was spin-coated at 2000 rpm. UV-vis spectroscopy for PTB7 with different vol % of DIO was performed by spin-coating the solution at 2000 rpm on the PEIE-coated glasses. UV-vis spectroscopy was performed by using a UV-vis spectrophotometer (Lambda 950 from PerkinElmer). Photoluminescence (PL) spectroscopy was performed on the pristine donor, the acceptor, and the blends by using a 490 nm TOPTICA class 3B diode laser to excite the films (kept in a vacuum) at a power of 5 mW for the blend and PC<sub>71</sub>BM whereas 0.5 mW for PTB7. A 610 nm long-pass filter was placed after the film to block the laser. The emission was collected by using a Shamrock SR-303i spectrograph with a gated integrated charge couple device (ICCD) from Andor. Height and phase AFM images for the blend films were performed by a Nanoscope IV multimode AFM from Veeco, and AFM on the films of PTB7 with different DIO vol % was measured by using the Dimension Icon AFM from Bruker. The AFM was recorded for the 3 μm × 3 μm window. TEM was performed at the Monash Centre for Electron Microscopy (MCEM) with a JEOL JEM 2100F field emission gun TEM in a bright-field mode. The domain size was calculated by measuring line profiles at randomized angles in the ImageJ software. NEXAFS spectra at the carbon edge were measured at the Australian Synchrotron at Soft X-ray beamline.<sup>44</sup> NEXAFS and GIWAXS films were prepared by spin-coating blend solution at the same parameters on Si/PEIE substrate. TEY was measured by the drain current flux at X-ray illumination. For each measurement, a new spot was chosen to avoid beam damage. The spectra were analyzed by using the Quick AS NEXAFS Tool (QANT).<sup>45</sup> The pre-edge of spectra was set to zero, and the intensity at 320 eV was set as 1. Double normalization of spectra was done by using a gold mesh, which was corrected by measuring the clean direct beam with a photodiode. Peak fitting and surface composition analysis were done by using the same software. GIWAXS measurements were performed at the small- and wide-angle X-ray scattering beamline at Australian Synchrotron.<sup>46</sup> The samples were irradiated by 15 keV X-rays at a fixed incident angle of 0.1° with an exposure time of 1 s. Data were processed by using a custom version of Nika implemented in IgorPro.<sup>47</sup> R-SoXS measurements were performed at the National Institute of Standards and Technology Spectroscopy Soft and Tender (SST-1) beamline of the National Synchrotron Light Source II. R-SoXS patterns were measured at different photon energies with 283.9 eV found to maximize materials contrast. Samples were measured in a transmission configuration under vacuum with scattering recorded on a 2D CCD camera (Greateyes). 2D R-SoXS patterns were converted to 1D line profiles by using a custom version of Nika implemented in IgorPro.<sup>47</sup> Scattering was measured at two sample-to-detector positions, with the low-*q* and high-*q* data stitched in software.

**Device Characterization.** Dark and Illuminated current–voltage (*I*–*V*) measurements were performed by using the Keithley 4200 semiconductor characterization system (SCS). The devices were illuminated by an LED solar simulator from ORIEL which was calibrated to 1 sun conditions (100 mW/cm<sup>2</sup>) at AM 1.5G. The EQE was measured by using a Bentham PVE300 that comprised a dual lamp source (Xenon and QTH lamp), and the lamp was calibrated by using a Si photodiode. Scanning photocurrent microscopy was performed by exciting the device, which was mounted on an Olympus IX73 microscope (60×, 0.71 NA), with a 638 nm TOPTICA laser diode. The laser beam of fluence 50 nW was chopped at 300 Hz and focused on the device by using a series of optical arrangements such that the spot size was ≈460 nm. The photocurrent signal and the phase were measured by using SR 830 lock-in amplifier, which was connected to the device and the chopper. The lock-in amplifier and the scanning stage were linked to Labview software such that the readings could be collected as a function of position.

**Simulation.** Finite difference time domain (FDTD) simulations using FDTD Solutions by Lumerical Inc. have been performed to mimic the experimental setup with a thin lens Gaussian source having 0.75 NA and wavelength of 633 nm to simulate the electric field in the device stack. The optical parameters (*n* and *k*) are measured for all the layers except the blend for which it is taken from the work of He et al.<sup>48</sup> The glass substrate is taken to be infinitely thick by using perfectly matched layer (PML) boundary conditions, and the source is inside the glass. For the waveguide mode simulations, 2-dimensional simulations are performed by using the waveguide mode as source with the direction of propagation along the *x*-axis (parallel to the interfaces) and the *y*-axis is perpendicular to the interfaces.

## ■ ASSOCIATED CONTENT

### Supporting Information

The Supporting Information is available free of charge at <https://pubs.acs.org/doi/10.1021/acsnm.0c02256>.

Energy level diagram and device architecture; illuminated *J*–*V*, dark *J*–*V*, EQE, AFM, TEM, R-SoXS, GIWAXS, NEXAFS, and PL for different additive concentrations in blend; knee voltage from dark *J*–*V*; methodology for calculating domain size from AFM and TEM; scanning photocurrent microscopy setup; hole-only and electron-only *J*–*V* plots; schematic of simulated device structure for FDTD simulations; absorbance for PTB7 film and solution for different DIO concentrations (PDF)

## ■ AUTHOR INFORMATION

### Corresponding Authors

Dinesh Kabra – Department of Physics, Indian Institute of Technology Bombay, Mumbai 400076, India; [orcid.org/0000-0001-5256-1465](https://orcid.org/0000-0001-5256-1465); Email: [dkabra@iitb.ac.in](mailto:dkabra@iitb.ac.in)

Christopher R. McNeill – Department of Materials Science and Engineering, Monash University, Clayton, Victoria 3800, Australia; [orcid.org/0000-0001-5221-878X](https://orcid.org/0000-0001-5221-878X); Email: [Christopher.mcneill@monash.edu](mailto:Christopher.mcneill@monash.edu)

### Authors

Urvashi Bothra – IITB-Monash Research Academy, IIT Bombay, Mumbai 400076, India; Department of Physics, Indian Institute of Technology Bombay, Mumbai 400076, India; Department of Materials Science and Engineering, Monash University, Clayton, Victoria 3800, Australia

Nakul Jain – Department of Physics, Indian Institute of Technology Bombay, Mumbai 400076, India; [orcid.org/0000-0001-6965-190X](https://orcid.org/0000-0001-6965-190X)

**Amelia C. Y. Liu** – School of Physics and Astronomy and Monash Centre for Electron Microscopy, Monash University, Clayton, Victoria 3800, Australia

**Abhinav Kala** – Department of Condensed Matter Physics & Material Science, Tata Institute of Fundamental Research, Mumbai 400076, India

**Wenchao Huang** – Department of Materials Science and Engineering, Monash University, Clayton, Victoria 3800, Australia; [orcid.org/0000-0003-4992-1727](https://orcid.org/0000-0003-4992-1727)

**Xuechen Jiao** – Department of Materials Science and Engineering, Monash University, Clayton, Victoria 3800, Australia; Australian Synchrotron, ANSTO, Clayton, Victoria 3168, Australia

**Eliot Gann** – Materials Measurement Science Division, National Institute of Standards and Technology, Gaithersburg, Maryland 20899, United States; [orcid.org/0000-0001-5570-8880](https://orcid.org/0000-0001-5570-8880)

**Venu Gopal Achanta** – Department of Condensed Matter Physics & Material Science, Tata Institute of Fundamental Research, Mumbai 400076, India; [orcid.org/0000-0002-2554-5475](https://orcid.org/0000-0002-2554-5475)

Complete contact information is available at:  
<https://pubs.acs.org/10.1021/acsnm.0c02256>

## Notes

The authors declare no competing financial interest.

## ACKNOWLEDGMENTS

We acknowledge the support from the NCPRE and IITB for device fabrication and the characterizations facility, respectively. This work was also supported by the DST-AISRF Grant DST/INT/AUS/P-74/2017 and SUNRISE-GCRF-RCUK. AFM was performed at Monash Centre for Nanofabrication (MCN) in the Victorian node of Australian National Fabrication Facility (ANFF). The authors acknowledge use of facilities within the Monash Centre for Electron Microscopy. GIWAXS and NEXAFS were performed at the SAXS/WAXS and Soft X-ray beamlines at the Australian Synchrotron, part of ANSTO. This research used the Spectroscopy Soft and Tender (SST-1) beamline of the National Synchrotron Light Source II, a U.S. Department of Energy (DOE) Office of Science User Facility operated for the DOE Office of Science by Brookhaven National Laboratory under Contract DE-SC0012704. C.R.M. acknowledges travel funding provided by the International Synchrotron Access Program (ISAP) managed by the Australian Synchrotron, part of ANSTO, and funded by the Australian Government. U.B. acknowledges IITB-Monash Research Academy for the scholarship. N.J. acknowledges the Council for Scientific and Industrial Research (CSIR), India, for the fellowship. W.H. has been supported by the Australian Government through the Australian Renewable Energy Agency (ARENA). A.C.Y.L. acknowledges support from the Australian Research Council (FT180100594).

## REFERENCES

(1) Song, X.; Gasparini, N.; Ye, L.; Yao, H.; Hou, J.; Ade, H.; Baran, D. Controlling Blend Morphology for Ultrahigh Current Density in Nonfullerene Acceptor-Based Organic Solar Cells. *ACS Energy Letters* **2018**, *3* (3), 669–676.

(2) Abdulrazzaq, O. A.; Saini, V.; Bourdo, S.; Dervishi, E.; Biris, A. S. Organic Solar Cells: A Review of Materials, Limitations, and Possibilities for Improvement. *Part. Sci. Technol.* **2013**, *31* (5), 427–442.

(3) Lu, L.; Zheng, T.; Wu, Q.; Schneider, A. M.; Zhao, D.; Yu, L. Recent Advances in Bulk Heterojunction Polymer Solar Cells. *Chem. Rev.* **2015**, *115* (23), 12666–731.

(4) Zhang, J.; Tan, H. S.; Guo, X.; Facchetti, A.; Yan, H. Material insights and challenges for non-fullerene organic solar cells based on small molecular acceptors. *Nature Energy* **2018**, *3* (9), 720–731.

(5) Zhang, X.; Tang, Y.; Yang, K.; Chen, P.; Guo, X. Additive-Free Non-Fullerene Organic Solar Cells. *ChemElectroChem.* **2019**, *6* (22), 5547–5562.

(6) Sun, H.; Guo, X.; Facchetti, A. High-Performance n-Type Polymer Semiconductors: Applications, Recent Development, and Challenges. *Chem.* **2020**, *6* (6), 1310–1326.

(7) Huang, W.; Gann, E.; Chandrasekaran, N.; Thomsen, L.; Prasad, S. K. K.; Hodgkiss, J. M.; Kabra, D.; Cheng, Y.-B.; McNeill, C. R. Isolating and quantifying the impact of domain purity on the performance of bulk heterojunction solar cells. *Energy Environ. Sci.* **2017**, *10* (8), 1843–1853.

(8) McNeill, C. R.; Greenham, N. C. Conjugated-Polymer Blends for Optoelectronics. *Adv. Mater.* **2009**, *21*, 3840–3850.

(9) Hedley, G. J.; Ward, A. J.; Alekseev, A.; Howells, C. T.; Martins, E. R.; Serrano, L. A.; Cooke, G.; Ruseckas, A.; Samuel, I. D. Determining the optimum morphology in high-performance polymer-fullerene organic photovoltaic cells. *Nat. Commun.* **2013**, *4*, 2867.

(10) Gao, F.; Inganäs, O. Charge generation in polymer-fullerene bulk-heterojunction solar cells. *Phys. Chem. Chem. Phys.* **2014**, *16* (38), 20291–304.

(11) Watkins, P. k.; Walker, A. B.; Verschoor, G. L. B. Dynamical Monte Carlo Modelling of Organic Solar Cells: The Dependence of Internal Quantum Efficiency on Morphology. *Nano Lett.* **2005**, *5* (5), 1814–1818.

(12) Erb, T.; Zhokhavets, U.; Gobsch, G.; Raleva, S.; Stühn, B.; Schilinsky, P.; Waldauf, C.; Brabec, C. J. Correlation Between Structural and Optical Properties of Composite Polymer/Fullerene Films for Organic Solar Cells. *Adv. Funct. Mater.* **2005**, *15* (7), 1193–1196.

(13) Liao, H.-C.; Ho, C.-C.; Chang, C.-Y.; Jao, M.-H.; Darling, S. B.; Su, W.-F. Additives for morphology control in high-efficiency organic solar cells. *Mater. Today* **2013**, *16* (9), 326–336.

(14) Chen, W.; Xu, T.; He, F.; Wang, W.; Wang, C.; Strzalka, J.; Liu, Y.; Wen, J.; Miller, D. J.; Chen, J.; Hong, K.; Yu, L.; Darling, S. B. Hierarchical nanomorphologies promote exciton dissociation in polymer/fullerene bulk heterojunction solar cells. *Nano Lett.* **2011**, *11* (9), 3707–13.

(15) Shin, N.; Richter, L. J.; Herzing, A. A.; Kline, R. J.; DeLongchamp, D. M. Effect of Processing Additives on the Solidification of Blade-Coated Polymer/Fullerene Blend Films via In-Situ Structure Measurements. *Adv. Energy Mater.* **2013**, *3* (7), 938–948.

(16) Bartelt, J. A.; Douglas, J. D.; Mateker, W. R.; Labban, A. E.; Tassone, C. J.; Toney, M. F.; Fréchet, J. M. J.; Beaujuge, P. M.; McGehee, M. D. Controlling Solution-Phase Polymer Aggregation with Molecular Weight and Solvent Additives to Optimize Polymer-Fullerene Bulk Heterojunction Solar Cells. *Adv. Energy Mater.* **2014**, *4* (9), 1301733.

(17) Lee, J. K.; Ma, W. L.; Brabec, C. J.; Yuen, J.; Moon, J. S.; Kim, J. Y.; Lee, K.; Bazan, G. C.; Heeger, A. J. Processing Additives for Improved Efficiency from Bulk Heterojunction Solar Cells. *J. Am. Chem. Soc.* **2008**, *130* (11), 3619–23.

(18) Li, N.; Brabec, C. J. Air-processed polymer tandem solar cells with power conversion efficiency exceeding 10%. *Energy Environ. Sci.* **2015**, *8* (10), 2902–2909.

(19) Tremolet de Villers, B. J.; O'Hara, K. A.; Ostrowski, D. P.; Biddle, P. H.; Shaheen, S. E.; Chabynyc, M. L.; Olson, D. C.; Kopidakis, N. Removal of Residual Diiodooctane Improves Photostability of High-Performance Organic Solar Cell Polymers. *Chem. Mater.* **2016**, *28* (3), 876–884.

(20) Doumon, N. Y.; Wang, G.; Qiu, X.; Minnaard, A. J.; Chiechi, R. C.; Koster, L. J. A. 1,8-diiodooctane acts as a photo-acid in organic solar cells. *Sci. Rep.* **2019**, *9* (1), 4350.

- (21) Jain, N.; Bothra, U.; Moghe, D.; Sadhanala, A.; Friend, R.; McNeill, C. R.; Kabra, D. Negative Correlation between Intermolecular vs Intramolecular Disorder in Bulk Heterojunction Organic Solar Cells. *ACS Appl. Mater. Interfaces* **2018**, *10* (51), 44576–44582.
- (22) Liang, Y.; Xu, Z.; Xia, J.; Tsai, S. T.; Wu, Y.; Li, G.; Ray, C.; Yu, L. For the bright future-bulk heterojunction polymer solar cells with power conversion efficiency of 7.4%. *Adv. Mater.* **2010**, *22* (20), E135–8.
- (23) Lou, S. J.; Szarko, J. M.; Xu, T.; Yu, L.; Marks, T. J.; Chen, L. X. Effects of additives on the morphology of solution phase aggregates formed by active layer components of high-efficiency organic solar cells. *J. Am. Chem. Soc.* **2011**, *133* (51), 20661–3.
- (24) Huang, W.; Gann, E.; Thomsen, L.; Dong, C.; Cheng, Y.-B.; McNeill, C. R. Unraveling the Morphology of High Efficiency Polymer Solar Cells Based on the Donor Polymer PBDTTT-EFT. *Adv. Energy Mater.* **2015**, *5* (7), 1–11.
- (25) Jain, N.; Chandrasekaran, N.; Sadhanala, A.; Friend, R. H.; McNeill, C. R.; Kabra, D. Interfacial disorder in efficient polymer solar cells: the impact of donor molecular structure and solvent additives. *J. Mater. Chem. A* **2017**, *5* (47), 24749–24757.
- (26) Collins, B. A.; Li, Z.; Tumbleston, J. R.; Gann, E.; McNeill, C. R.; Ade, H. Absolute Measurement of Domain Composition and Nanoscale Size Distribution Explains Performance in PTB7:PC71BM Solar Cells. *Adv. Energy Mater.* **2013**, *3* (1), 65–74.
- (27) Kouijzer, S.; Michels, J. J.; van den Berg, M.; Gevaerts, V. S.; Turbiez, M.; Wienk, M. M.; Janssen, R. A. Predicting morphologies of solution processed polymer:fullerene blends. *J. Am. Chem. Soc.* **2013**, *135* (32), 12057–67.
- (28) Tang, B.; Liu, J.; Cao, X.; Zhao, Q.; Yu, X.; Zheng, S.; Han, Y. Restricting the liquid–liquid phase separation of PTB7-Th:PF12TBT:PC71BM by enhanced PTB7-Th solution aggregation to optimize the interpenetrating network. *RSC Adv.* **2017**, *7* (29), 17913–17922.
- (29) van Franeker, J. J.; Turbiez, M.; Li, W.; Wienk, M. M.; Janssen, R. A. A real-time study of the benefits of co-solvents in polymer solar cell processing. *Nat. Commun.* **2015**, *6*, 6229.
- (30) Zusan, A.; Gieseking, B.; Zerson, M.; Dyakonov, V.; Magerle, R.; Deibel, C. The effect of diiodooctane on the charge carrier generation in organic solar cells based on the copolymer PBDTTT-C. *Sci. Rep.* **2015**, *5*, 8286.
- (31) Kim, W.; Kim, J. K.; Kim, E.; Ahn, T. K.; Wang, D. H.; Park, J. H. Conflicted Effects of a Solvent Additive on PTB7:PC71BM Bulk Heterojunction Solar Cells. *J. Phys. Chem. C* **2015**, *119* (11), 5954–5961.
- (32) Chandrasekaran, N.; Gann, E.; Jain, N.; Kumar, A.; Gopinathan, S.; Sadhanala, A.; Friend, R. H.; Kumar, A.; McNeill, C. R.; Kabra, D. Correlation between Photovoltaic Performance and Interchain Ordering Induced Delocalization of Electronics States in Conjugated Polymer Blends. *ACS Appl. Mater. Interfaces* **2016**, *8* (31), 20243–50.
- (33) Duan, C.; Peng, Z.; Colberts, F. J. M.; Pang, S.; Ye, L.; Awartani, O. M.; Hendriks, K. H.; Ade, H.; Wienk, M. M.; Janssen, R. A. J. Efficient Thick-Film Polymer Solar Cells with Enhanced Fill Factors via Increased Fullerene Loading. *ACS Appl. Mater. Interfaces* **2019**, *11* (11), 10794–10800.
- (34) Reid, D. R.; Jackson, N. E.; Bourque, A. J.; Snyder, C. R.; Jones, R. L.; de Pablo, J. J. Aggregation and Solubility of a Model Conjugated Donor-Acceptor Polymer. *J. Phys. Chem. Lett.* **2018**, *9* (16), 4802–4807.
- (35) Hoven, C. V.; Dang, X. D.; Coffin, R. C.; Peet, J.; Nguyen, T. Q.; Bazan, G. C. Improved performance of polymer bulk heterojunction solar cells through the reduction of phase separation via solvent additives. *Adv. Mater.* **2010**, *22* (8), E63–6.
- (36) Rivnay, J.; Mannsfeld, S. C.; Miller, C. E.; Salleo, A.; Toney, M. F. Quantitative determination of organic semiconductor microstructure from the molecular to device scale. *Chem. Rev.* **2012**, *112* (10), 5488–519.
- (37) Ho, C. H. Y.; Dong, Q.; Yin, H.; Leung, W. W. K.; Yang, Q.; Lee, H. K. H.; Tsang, S. W.; So, S. K. Impact of Solvent Additive on Carrier Transport in Polymer:Fullerene Bulk Heterojunction Photovoltaic Cells. *Adv. Mater. Interfaces* **2015**, *2* (12), 1500166.
- (38) Kniepert, J.; Lange, I.; Heidbrink, J.; Kurpiers, J.; Brenner, T. J. K.; Koster, L. J. A.; Neher, D. Effect of Solvent Additive on Generation, Recombination, and Extraction in PTB7:PCBM Solar Cells: A Conclusive Experimental and Numerical Simulation Study. *J. Phys. Chem. C* **2015**, *119* (15), 8310–8320.
- (39) Kabra, D.; Shriram, S.; Vidhyadhiraja, N. S.; Narayan, K. S. Charge carrier dynamics in organic semiconductors by position dependent optical probing. *J. Appl. Phys.* **2007**, *101* (6), 064510.
- (40) Kabra, D.; Narayan, K. S. Direct Estimate of Transport Length Scales in Semiconducting Polymers. *Adv. Mater.* **2007**, *19* (11), 1465–1470.
- (41) Lee, J. Y.; Roth, S.; Park, Y. W. Anisotropic field effect mobility in single crystal pentacene. *Appl. Phys. Lett.* **2006**, *88* (25), 252106.
- (42) Scharsich, C.; Lohwasser, R. H.; Sommer, M.; Asawapirom, U.; Scherf, U.; Thelakkat, M.; Neher, D.; Köhler, A. Control of aggregate formation in poly(3-hexylthiophene) by solvent, molecular weight, and synthetic method. *J. Polym. Sci., Part B: Polym. Phys.* **2012**, *50* (6), 442–453.
- (43) Kim, Y. J.; Ahn, S.; Wang, D. H.; Park, C. E. A Mechanistic Understanding of a Binary Additive System to Synergistically Boost Efficiency in All-Polymer Solar Cells. *Sci. Rep.* **2015**, *5*, 18024 1–13.
- (44) Cowie, B. C. C.; Tadich, A.; Thomsen, L.; Garrett, R.; Gentle, I.; Nugent, K.; Wilkins, S. The Current Performance of the Wide Range (90–2500 eV) Soft X-ray Beamline at the Australian Synchrotron. *AIP Conf. Proc.* **2009**, *1234* (1), 307–310.
- (45) Gann, E.; McNeill, C. R.; Tadich, A.; Cowie, B. C.; Thomsen, L. Quick AS NEXAFS Tool (QANT): a program for NEXAFS loading and analysis developed at the Australian Synchrotron. *J. Synchrotron Radiat.* **2016**, *23* (1), 374–80.
- (46) Kirby, N. M.; Mudie, S. T.; Hawley, A. M.; Cookson, D. J.; Mertens, H. D. T.; Cowieson, N.; Samardzic-Boban, V. A low-background-intensity focusing small-angle X-ray scattering undulator beamline. *J. Appl. Crystallogr.* **2013**, *46* (6), 1670–1680.
- (47) Ilavsky, J. Nika: software for two-dimensional data reduction. *J. Appl. Crystallogr.* **2012**, *45*, 324–328.
- (48) He, Z.; Zhong, C.; Su, S.; Xu, M.; Wu, H.; Cao, Y. Enhanced power-conversion efficiency in polymer solar cells using an inverted device structure. *Nat. Photonics* **2012**, *6* (9), 591–595.